This is the peer-reviewed, final accepted version for American Mineralogist, published by the Mineralogical Society of America.
The published version is subject to change. Cite as Authors (Year) Title. American Mineralogist, in press.
DOI: https://doi.org/10.2138/am-2022-8081. http://www.minsocam.org/

Revision 2

Sound speed and refractive index of amorphous $CaSiO_3$ upon pressure cycling to 40 GPa

Zachary M. Geballe[1,2], Sarah M. Arveson[1], Sergio Speziale[3], Raymond Jeanloz[1,4]

1. Department of Earth and Planetary Sciences, University of California, Berkeley, CA 94720, USA
2. Earth and Planets Laboratory, Carnegie Institution of Washington, Washington, DC 20015, USA
3. GFZ German Research Center for Geosciences, Potsdam, Germany
4. Miller Institute, University of California, Berkeley, CA 94720, USA

Abstract

Brillouin spectroscopy at room temperature and pressure up to 40 GPa documents nearly identical elasticity and refractive index of amorphous $CaSiO_3$ created by two different methods: temperature-quenching the melt at ambient pressure, and pressure-amorphizing crystalline wollastonite at room temperature. We find reproducible hysteresis of 0 to 8% on pressure cycling that is small relative to the 30% to 60% changes in shear and longitudinal wave velocities over this pressure range. Together with observed changes in refractive index and previous results from Raman spectroscopy, these measurements reveal a continuous and reversible change in atomic-packing induced by pressure. Unlike many other silicate glasses, amorphous $CaSiO_3$ exhibits highly reproducible properties, behaving smoothly and reversibly under pressure cycling and possessing similar structure and elasticity regardless of synthesis paths for the starting material, which suggests that the amorphous solid may mimic the liquid over the pressure range investigated.

1. Introduction

Knowledge of the density and elasticity of silicate melts at high pressures is important for understanding the deep Earth, because buoyancy drives melt migration, which in turn plays a key role in the thermal-chemical evolution of our planet. Laboratory measurements of melt properties at simultaneously high temperatures and pressures are challenging, however (Sanloup et al., 2013; Ahart et al., 2014; Andrault et al., 2020). We can instead examine silicate glasses at room temperature, which provide frozen snapshots of silicate melt structure under compression and can be studied using a wide range of probes up to high pressures (Murakami and Bass, 2010, 2011; Petitgirard et al., 2017; Kono et al., 2018; Mysen and Richet, 2019). The primary concern with this approach is in establishing the degree to which the kinetically frozen structure of the glass at 300 K mimics the atomic-packing configuration of the melt, as reflected in such bulk properties as density and elasticity. Reversibility upon compression and decompression is a pre-requisite for inferring that relevant degrees of freedom remain unhindered in the glass at 300 K. For example, it is known that some properties of SiO_2 and $MgSiO_3$ glasses show evidence of kinetic hindrance (i.e., lack of reversibility upon compression and decompression) and are therefore not entirely representative of the properties of the corresponding melts (Grimsditch, 1984; Sanchez-Valle and Bass, 2010). In contrast, minimal hysteresis has been observed in Raman spectroscopy, IR absorption spectroscopy, x-ray diffraction, and x-ray emission spectroscopy of amorphous $CaSiO_3$, on compression and decompression (Kubicki et al., 1992; Serghiou et al., 2000; Shimoda et al., 2005; Shim and Catalli, 2009). This reversibility suggests that $CaSiO_3$ glass may reflect the physical properties (e.g., density, elasticity, structure) of the melt over a wide range of pressure.

To further compare amorphous $CaSiO_3$ samples that have experienced different pressure-temperature histories, we characterize the elasticity and refractive index of amorphous $CaSiO_3$ at ambient temperature to ~40 GPa using two different types of samples: one formed by solid-state pressure-induced amorphization, and the other formed by thermal quenching from the melt at ambient pressure. We also make measurements during multiple cycles of compression and decompression. The apparent redundancy in measurements is by design; we generate high-pressure amorphous $CaSiO_3$ from multiple starting materials and use multiple compression

cycles as a way to check both the reproducibility and reversibility of properties. To be clear, we refer to a sample lacking long-range crystalline order as being amorphous and reserve the term glass for the thermally quenched melt.

2. Experimental Method

Melt-quenched material from two different sources gave indistinguishable results and will therefore be described as the "glass" in all figures and subsequent text: the glass used by Richet et al. (1993) and the glass used by Kubicki et al. (1992). The glasses were polished on two sides to ~20 µm thickness, placed in the sample chambers of diamond-anvil cells with 350 µm culets and rhenium gaskets, and surrounded by an argon pressure medium.

Natural wollastonite crystals from Riverside, CA, with ~millimeter grain size were ground into a fine powder (< 3 µm grain size) with a mortar and pestle. The powder was loaded into the 140 µm diameter hole of a rhenium gasket pre-indented to 30 µm thickness. The culet diameter of the diamond anvils was 350 µm.

The crystalline powder was pressure-amorphized and studied by the following procedure. The powder sample was pressure-cycled twice to ~40 GPa with no pressure medium, re-loaded into a diamond cell with a methanol-ethanol-water pressure medium (mass ratio 16:3:1), compressed to 42 GPa and decompressed to 0 GPa. The powder became mostly amorphous upon compression to 35 GPa, and was almost completely amorphous after three pressure cycles to ~40 GPa.

Amorphization was confirmed with x-ray diffraction patterns collected during the first compression and after the final decompression at beamline 12.2.2 of the ALS, using 25 keV x-rays focused to a 10 µm spot size (Yan et al., 2010). Amorphization was indicated by a nearly-complete disappearance of crystalline x-ray diffraction peaks (Fig. 1). This is consistent with the previous detection of partial amorphization between 17 and 26 GPa using energy dispersive x-ray diffraction (Serghiou and Hammack, 1993).

Note that we also attempted to study single crystal wollastonite, but sets of parallel cracks developed in the sample at pressure between 2 and 3 GPa, preventing detection of Brillouin peaks. No data for single crystal wollastonite are reported here.

Brillouin spectra were collected in 40° equal-angle forward-scattering, as well as 180° backscattering at UC Berkeley, using the following optical path: the beam from a 532 nm Verdi laser was expanded to 10 mm using two lenses, apertured using a 1.5 mm vertical slit, and focused onto the sample using a 50 mm focal length achromat. Fig. 2 shows an optical image of a sample in a diamond anvil cell with the laser focused onto it. Scattered light was collected by an identical achromat, apertured with a 1.5 mm vertical slit, and focused onto the pinhole of a Sandercock Tandem Fabry-Perot Interferometer using a 40 cm focal length focusing lens. Typically, one compression-decompression cycle was completed over the course of one to three days. The pressure was changed approximately once per hour.

Longitudinal and transverse acoustic velocities, V_P and V_S, are determined from the frequency shifts of Brillouin peaks in the forward scattering geometry, Δf, using the equation:

$$V = \frac{\lambda_0 \Delta f}{2\sin(\theta/2)} \quad (1)$$

where λ_0 is the laser wavelength (532 nm), and θ is the scattering angle (40°) (Whitfield et al., 1976). The product of refractive index, n, and longitudinal velocity is determined from the frequency shift in the backscatter direction, $\Delta f_{P,b}$:

$$nV_P = \frac{\lambda_0 \Delta f_{P,b}}{2} \quad (2)$$

Dividing (2) by (1),

$$n = \sin(\theta/2)\frac{\Delta f_{P,b}}{\Delta f_P} \quad (3)$$

where the subscript P refers to longitudinal wave, and b refers to backscatter geometry (Shimizu et al., 1998).

The accuracy of the system was found to be ~1%, calibrated using the Brillouin spectra from single crystals of quartz at ambient pressure and confirmed by measuring $CaSiO_3$ glass between 0 and 20 GPa at GFZ in Potsdam using 60° equal angle scattering geometry. Scatter in peak positions collected from different rotations about the diamond cell axis was 0.5 to 1%.

Pressure was measured from the fluorescence lineshift of two to four rubies spheres placed near the edge of the gasket hole (Mao et al., 1986). All high-pressure measurements were obtained at room temperature.

3. Results

3.1 Velocity and refractive index

The main result of the Brillouin measurements is that melt-quenched and solid-state amorphized samples exhibit identical velocities upon compression and decompression, with up to 8% hysteresis, and the results are reproducible upon multiple quasi-hydrostatic pressure-cycling to ~40 GPa (Fig. 3a). In contrast, measurements under non-hydrostatic loading show a systematic reduction by ~4% in velocity (see the Appendix for details); the main text describes the quasi-hydrostatic data only.

The hysteresis in V_P and V_S is a small fraction of the total change across the pressure range studied here: 7% and 8% maximum hysteresis compared to 60% and 30% changes in V_P and V_S, respectively (Fig. 3a). Moreover, V_P and V_S increase smoothly with pressure, and no kinks are observed in velocity-pressure curves upon compression or decompression (Fig. 3a). As a percentage of the overall change, hysteresis is largest for the index of refraction, *n*. During one decompression run, *dn/dP* is negative in the pressure range ~20 to 35 GPa (Fig 3b).

3.2 Lower bound on density

The bulk sound speed, V_ϕ, can be calculated for each data point by

$$V_\phi = \sqrt{{V_P}^2 - \frac{4}{3}{V_S}^2} \tag{4}$$

The result, shown in Fig. 4, is fitted to a polynomial, $V_\phi = 4.96 + 0.096P - 0.00043P^2$, and integrated to find a lower bound on density change:

$$\int_0^P \frac{1}{{V_\phi}^2} dP = \int_0^P \frac{\rho}{K_{S,GHz}} dP \leq \int_0^P \frac{\rho}{K_S} dP \leq \int_0^P \frac{\rho}{K_T} dP \leq \Delta\rho \tag{5}$$

The first inequality in equation (5) results from the fact that the adiabatic bulk modulus at GHz frequency, $K_{S,GHz}$, which is probed with Brillouin spectroscopy, may be larger than the low frequency version, K_S, due to phonon dispersion. The second inequality results from the fact that K_S is larger than the isothermal bulk modulus, K_T, which controls compression in a diamond cell. Their ratio, K_S/K_T, equals $(1 + \alpha\gamma T)$, where α is the coefficient of thermal expansion and γ is the Grüneisen parameter. The value $\alpha\gamma T$ is of order 1% at room temperature. The third inequality is due to possible discontinuous structural changes, the analog of crystal-structural

phase transitions for crystalline materials. If they take place in the amorphous samples, these structural transitions cause $\Delta\rho/\Delta P$ at relatively large strain amplitude (i.e. compression by tightening of the diamond cell) to be larger than ρ/K_T at small strain amplitude (i.e. the strain amplitudes associated with phonons and measured by Brillouin spectroscopy).

Adding $\Delta\rho$ to the density at ambient pressure, ρ_0, we determine a lower bound for the density at high pressure,

$$\rho \geq \rho_0 + \int_0^P \frac{1}{V_\phi{}^2} dP \qquad (6)$$

The result is plotted in Fig. 5 and compared to two values for similarly low-density crystalline polymorphs, wollastonite and walstromite, as well as to the high-density polymorph perovskite. Fig. 5 shows that the density of amorphous $CaSiO_3$ increases by at least 33% from ambient pressure to 40 GPa. Amorphous $CaSiO_3$ is much more compressible than calcium perovskite over this range.

In fact, amorphous $CaSiO_3$ may be more compressible than suggested by the lower bound determined here (Fig. 5). For comparison, Petitgirard et al. (2015) argues that structural relaxation in $MgSiO_3$ causes an additional 20% density increase in the pressure range 0-35 GPa, in addition to the 20% density increase inferred by integrating the Brillouin data from Sanchez-Valle and Bass (2010).

4. Discussion

4.1 Relative stability of amorphous $CaSiO_3$

Four observations characterize the metastability of amorphous $CaSiO_3$ at room temperature and pressures from 0 to ~40 GPa: (1) limited hysteresis in V_P and V_S; (2) smooth changes in velocity vs. pressure (i.e., no kinks); (3) continuous pressure variation of Raman and infrared spectra of melt-quenched amorphous $CaSiO_3$ observed in previous studies (Kubicki et al., 1992; Shim and Catalli, 2009); and (4) the nearly identical sound speeds observed here and Raman spectra observed by Serghiou et al. (2000) for melt-quenched $CaSiO_3$ and compression-amorphized $CaSiO_3$. Table 1 and Fig. 7 show that observations (1) and (2) for amorphous $CaSiO_3$ clearly differ from the behavior observed for amorphous $MgSiO_3$ and SiO_2 under pressure. This

difference between $CaSiO_3$ and other silicates may be associated with the relatively small density difference between amorphous $CaSiO_3$ and its ambient pressure crystalline polymorph, wollastonite (Table 1). In fact, it is possible that the reproducible properties of different amorphous $CaSiO_3$ samples, regardless of synthesis path (solid-state amorphization vs. thermally quenched melt), and the similarity of density between amorphous solid and crystal may both reflect a local structure that is common to liquid, crystal and solid amorphous $CaSiO_3$, and which is energetically-favorable and accessible from many temperature routes. This interpretation is an extension of the proposal of Ai and Lange (2008) that liquid $CaSiO_3$ has a local structure close to that of the pyroxenoid crystal from which it melts.

To illustrate the meaning of the relative (meta)stability of amorphous $CaSiO_3$, we describe the relevant energy landscape (Fig. 6). With compression of at least 33% up to 40 GPa, the energies of crystalline and amorphous states increase substantially. For example, the integral of PdV from ambient pressure to 40 GPa is at least 2.8 eV/atom for amorphous $CaSiO_3$. At all pressures from 0 to 40 GPa, potential energy barriers of at least k_BT (25 meV per degree of freedom) block the amorphous sample from finding a deeper local minimum of a significantly different structure. Upon decompression, the sample presumably follows the same transformational path, with a small amount of hysteresis. (Alternatively, it is possible that the decompression path is slightly different, as suggested by the one decompression run in which dn/dP is negative in the pressure range ~20 to 35 GPa.) Upon further decompression, the sample finds its way back to the original potential energy minimum at ambient pressure. Moreover, the same local minima of amorphous structures are reached by room temperature compression of wollastonite powder, meaning the energy barrier between wollastonite and amorphous $CaSiO_3$ is less than ~25 meV per degree of freedom at ~40 GPa and room temperature, as shown in schematic C of Fig. 6.

Amorphous SiO_2, by contrast, becomes trapped in a high-pressure structure upon decompression to ambient pressure at 300 K, with distinct intermediate-range structure (but identical nearest-neighbor coordination) relative to the starting material. High-temperature annealing is required to reverse the changes in structure and bulk properties (Grimsditch, 1986). The behavior of amorphous $MgSiO_3$ is in-between the behaviors exhibited by amorphous

$CaSiO_3$ and SiO_2. The kinks in velocity versus pressure and the reversibility of sound speed with 12% hysteresis upon pressure cycling of $MgSiO_3$ suggest the presence of a significant transition to a high-pressure amorphous structure upon compression, which is reversible upon decompression to ambient pressure.

4.2 Structural changes with pressure

Raman spectroscopy is a sensitive probe of the structure of amorphous $CaSiO_3$ (Serghiou et al., 2000; Shim and Catalli, 2009). Upon room temperature compression, Shim and Catalli (2009) document the gradual disappearance of bending modes associated with SiO_4 tetrahedra and appearance of a stretching mode near 800 cm^{-1} in the pressure range ~20 to 50 GPa. Upon decompression, the reverse occurs. This suggests a gradual and reversible structural transition from mostly 4-fold coordinated Si to a mixture of 4-fold and higher coordinated Si at high pressures (Shim and Catalli, 2009). Index of refraction measurements in the present study are consistent with this structural change. The index of refraction increases due to increasing density up to ~20 GPa, but from 20 to 40 GPa the density change is countered by decreasing polarizability as silicon changes from covalent toward ionic bonding (tetrahedral to octahedral configurations) (Fig. 3b). The change in slope at 30 GPa is subtle upon compression, but more dramatic on decompression at 20 GPa. Hence, not only do amorphous $CaSiO_3$ samples synthesized by different methods exhibit the same bulk and vibrational properties at ambient conditions, but they are gradually transformed to a new, higher-coordination structure under pressure that then reverts upon return to ambient conditions. The final, recovered state of the sample is indistinguishable by Brillouin and Raman spectroscopy from the starting material.

In addition to the changes upon pressure cycling at room temperature, subtle variations in the structure of amorphous $CaSiO_3$ have been documented during pressure cycling at high-temperature. Shimoda et al. (2005) find that amorphous $CaSiO_3$ densifies by 3%, and one of its Raman modes changes by a small amount (6 cm^{-1}) upon cycling pressure to 7.5 GPa at 500 °C. No change is detected in x-ray emission, x-ray diffraction or IR absorption spectroscopy. Shimoda et al. (2005) suggest that the densification is due to a change in the intermediate range scale, such as a decrease in cluster size, but that any change "in Si-O-Si bond angle is very

small". The slight changes observed upon cycling to 7.5 GPa and 500 °C suggest that high temperature can induce minor irreversible structural relaxation of amorphous $CaSiO_3$.

4.3 Alternate synthesis routes for amorphous $CaSiO_3$

A third route to synthesizing amorphous $CaSiO_3$ is by room-temperature decompression of the perovskite phase that is formed above 15 GPa at elevated temperatures (Ringwood and Major, 1971; Kanzaki et al., 1991). Although less is known about this decompression-amorphized material, measurements of the index of refraction and of the ^{29}Si NMR chemical shift provide evidence that it is similar if not identical to the conventional (melt-quenched) and pressure-amorphized materials examined here (Table 2).

A fourth route to synthesizing amorphous $CaSiO_3$ is a variation on the conventional method: thermally quenching a high-pressure melt. While this route has only been used in one study we know of, the ambient-pressure Raman spectrum after decompressing this glass is similar to that of the conventional glass (thermally quenched from the melt at ambient pressure) and the pressure-amorphized wollastonite (Serghiou et al., 2000).

4.4 Comparison with other amorphous solids

Altogether, we find that amorphous $CaSiO_3$ exhibits especially reproducible properties at ambient conditions and under pressure cycling, with four synthesis routes generating amorphous $CaSiO_3$ having nearly identical elastic and vibrational properties (Table 1).

Reproducibility upon pressure cycling and insensitivity to synthesis route has also been documented in other glasses, including H_2O (Bowron et al., 2006; Klug et al., 1989; Mishima, 1994; Mishima et al., 1984), As_2O_3 (Soignard et al., 2008), $GaSe_4$ (Kalkan et al., 2014), and AsSe (Ahmad et al., 2016). In addition, amorphous GeO_2 and amorphous Be_2O_3 have been pressure cycled to and from high pressure amorphous structures, but have not been pressure-amorphized from their crystalline forms to-date (Fujisawa et al., 1994; Wolf et al., 1992; Prakapenka et al., 2004; Smith et al., 1995; Grimsditch et al., 1988; Cherednichenko et al., 2016; Nicholas et al., 2004). Finally, amorphous SiO_2 can be synthesized by compression amorphization, but after pressure cycling, high-temperature annealing is required to reestablish

the low-pressure structure of silica glass (Grimsditch, 1984, 1986; Grimsditch et al., 1994; Hemley et al., 1988).

5. Implications

The structure and bulk properties of amorphous $CaSiO_3$ are reproducible and reversible under pressure, especially as compared with results for other silicate glasses. This suggests that a local structure is common to amorphous, crystalline, and liquid $CaSiO_3$. Moreover, the reproducibility of bulk properties of amorphous $CaSiO_3$ at pressures from ambient to 40 GPa suggests that the amorphous solid may mimic the liquid over this pressure range.

6. Acknowledgements

We thank Pascal Richet, Rus Hemley, and Bjorn Mysen for providing us samples of $CaSiO_3$ glass and Tim Teague for providing us with natural crystalline wollastonite. We thank Rebecca Lange, Dan Shim, David Chandler, Rus Hemley and Bjorn Mysen for helpful discussions. Work was supported by the University of California, including the Miller Institute for Basic Research in Science, and the US DOE/NNSA under award DE-NA-0002006, CDAC. The Advanced Light Source is supported by the U.S. DOE under Contract No. DE-AC02-05CH11231 at Lawrence Berkeley National Laboratory.

Appendix: Effect of non-hydrostatic stress

The velocities and refractive indices presented in the main text were measured in samples compressed quasi-hydrostatically during seven pressure cycles, yielding ±2% scatter in V_P, V_S, and n. Data were omitted from the main text from the three pressure cycles in which the sample was pressed against both diamonds without a significant layer of soft medium to distribute stress. Figs. 8-9 show these data.

Two of the previously-omitted pressure cycles were from the wollastonite powder sample that was purposefully loaded without a pressure medium. One was the second pressure cycle of a sample loaded with an argon medium. In this case, when the laser was focused on the glass sample, there was no Brillouin peak from argon (i.e. no peak at ~8 GHz in the cyan spectrum in

Fig. 9), meaning that a negligibly thin layer of argon separates the sample from the diamond anvils. Instead, the majority of the argon must have been squeezed away from the sample region during the two pressure cycles. During these three compression runs without a substantial pressure medium, Fig. 8 shows that non-hydrostatic stress (and resulting strain) cause a 4% systematic reduction of sound speed between 20 and 40 GPa.

We hypothesize that changes in atomic packing (coordination changes) during non-hydrostatic compression cause the observed sound-speed reduction; shear stresses activate rearrangements of atoms into denser packings, which cause decreases in V_P and V_S (Fig. 8). This hypothesis is also consistent with most of the decompression data: sound speeds during decompression following non-hydrostatic compression are slightly lower than other decompression data between 40 and 20 GPa (empty cyan squares in Fig. 8). Nonetheless, as in the case of quasi-hydrostatic compression, sound speeds return to their original values upon decompression to 0 GPa.

References

Ahart, M., Karandikar, A., Gramsch, S., Boehler, R., Hemley, R.J., 2014. High P–T Brillouin scattering study of H_2O melting to 26 GPa. High Pressure Research 34, 327-336. DOI:10.1080/08957959.2014.946504.

Ahmad, A.S., Glazyrin, K., Liermann, H.P., Franz, H., Wang, X.D., Cao, Q.P., Zhang, D.X., Jiang, J.Z., 2016. Breakdown of intermediate range order in AsSe chalcogenide glass. Journal of Applied Physics 120, 145901. DOI:10.1063/1.4964798.

Ai, Y., Lange, R.A., 2008. New acoustic velocity measurements on CaO-MgO-Al_2O_3-SiO_2. Journal of Geophysical Research 113, B04203. DOI:10.1029/2007JB005010.

Akaogi, M., Yano, M., Tejima, Y., Iijima, M., Kojitani, H., 2004. High-pressure transitions of diopside and wollastonite: phase equilibria and thermochemistry of $CaMgSi_2O_6$, $CaSiO_3$ and $CaSi_2O_5$-$CaTiSiO_5$ system. Physics of the Earth and Planetary Interiors 143, 145–156. DOI:10.1016/j.pepi.2003.08.008.

Andrault, D., Morard, G., Garbarino, G., Mezouar, M., Bouhifd, M.A., Kawamoto, T., 2020. Melting behavior of SiO_2 up to 120 GPa. Physics and Chemistry of Minerals 47, 10. DOI:10.1007/s00269-019-01077-3.

Bowron, D.T., Finneya, J.L., Hallbrucker, A., Kohl, I., Loerting, T., Mayer, E., Soper, A.K., 2006. The local and intermediate range structures of the five amorphous ices at 80 K and ambient pressure: A Faber-Ziman and Bhatia-Thornton analysis. Journal of Chemical Physics 194502. DOI:10.1063/1.2378921.

Brückner, R., 1970. Properties and structure of vitreous silica. I. Journal of Non Crystalline Solids 5, 123–175. DOI:10.1016/0022-3093(70)90190-0.

Cherednichenko, K.A., Le Godec, Y., Kalinko, A., Mezouar, M., Solozhenko, V.L., 2016. Orthorhombic boron oxide under pressure: In situ study by X-ray diffraction and Raman scattering. Journal of Applied Physics 120, 175901. DOI:10.1063/1.4966658.

Fujisawa, H., Ito, E., Ohtaka, O., Yamanaka, T., 1994. Elastic wave velocities of high density pressure-induced amorphous GeO_2. Geophysical Research Letters 21, 1499-1502. DOI:10.1029/94GL01013.

Grimsditch, M., 1984. Polymorphism in Amorphous SiO_2. Physical Review Letters 52, 2379–

2381. DOI:10.1103/PhysRevLett.52.2379.

Grimsditch, M., 1986. Annealing and relaxation in the high-pressure phase of amorphous SiO_2. Physical Review B 34, 4372–4373. DOI:10.1103/PhysRevB.34.4372.

Grimsditch, M., Bhadra, R., Meng, Y., 1988. Brillouin scattering from amorphous materials at high pressures. Physical Review B 38, 7836–7838. DOI:10.1103/PhysRevB.38.7836.

Grimsditch, M., Popova, S., Brazhkin, V.V., Voloshin, R.N., 1994. Temperature-induced amorphization of SiO_2 stishovite. Physical Review B 50, 984–986. DOI:10.1103/physrevb.50.12984.

Hemley, R.J., Jephcoat, A.P., Mao, H.K., Ming, L.C., Manghnani, M.H., 1988. Pressure-induced amorphization of crystalline silica. Nature 334, 52–54. DOI:10.1038/334052a0.

Joswig, W., Paulus, E.F., Winkler, B., Milman, V., 2003. The crystal structure of $CaSiO_3$-walstromite, a special isomorph of wollastonite-II. Zeitschrift fur Kristallographie 218, 811–818. DOI:10.1524/zkri.218.12.811.20547.

Kalkan, B., Dias, R.P., Yoo, C.S., Clark, S.M., Sen, S., 2014. Polyamorphism and Pressure-Induced Metallization at the Rigidity Percolation Threshold in Densified $GeSe_4$ Glass. The Journal of Physical Chemistry C 118, 5110–5121. DOI:10.1021/jp4108602.

Kanzaki, M., Stebbins, J.F., Xue, X., 1991. Characterization of quenched high pressure phases in $CaSiO_3$ system by XRD and ^{29}Si NMR. Geophysical Research Letters 18, 463–466. DOI:10.1029/91GL00463.

Klug, D.D., Handa, Y.P., Tse, J.S., Whalley, E., 1989. Transformation of ice VIII to amorphous ice by “melting” at low temperature. Journal of Chemical Physics 90, 2390–2392. DOI:10.1063/1.455981.

Kono, Y., Shibazaki, Y., Kenney-Benson, C., Wang, Y., Shen, G., 2018. Pressure-induced structural change in $MgSiO_3$ glass at pressures near the Earth’s core-mantle boundary. Proceedings of the National Academy of Science 115, 1742–1747. DOI:10.1073/pnas.1716748115.

Kubicki, J.D., Hemley, R.J., Hofmeister, A.M., 1992. Raman and infrared study of pressure-induced structural changes in $MgSiO_3$, $CaMgSi_2O_6$, and $CaSiO_3$ glasses. American Mineralogist 77, 258–269.

Mao, H.K., Xu, J., Bell, P., 1986. Calibration of the Ruby Pressure Gauge to 800 kbar Under

Quasi-Hydrostatic Conditions. Journal of Geophysical Research 91, 4673–4676. DOI:10.1029/JB091iB05p04673.

Mishima, O., 1994. Reversible first-order transition between two H_2O amorphs at ∼0.2 GPa and ∼135 K. Journal of Chemical Physics 100, 5910–5912. DOI:10.1063/1.467103.

Mishima, O., Calvert, L.D., Whalley, E., 1984. Melting ice I at 77 K and 10 kbar: a new method of making amorphous solids. Nature 310, 393–395. DOI:10.1038/310393a0.

Murakami, M., Bass, J.D., 2010. Spectroscopic Evidence for Ultrahigh-Pressure Polymorphism in SiO_2 Glass. Physical Review Letters 104, 025504. DOI:10.1103/PhysRevLett.104.025504.

Murakami, M., Bass, J.D., 2011. Evidence of denser $MgSiO_3$ glass above 133 gigapascal (GPa) and implications for remnants of ultradense silicate melt from a deep magma ocean. Proceedings of the National Academy of Science 108, 17286–17289. DOI:10.1073/pnas.1109748108.

Mysen, B., Richet, P., 2019. Silicate Glasses and Melts (Second Edition). Second edition ed., Elsevier, Amsterdam. DOI:10.1016/B978-0-444-63708-6.09993-2.

Nicholas, J., Sinogeikin, S., Kieffer, J., Bass, J., 2004. Spectroscopic Evidence of Polymorphism in Vitreous B_2O_3. Physical Review Letters 21, 215701. DOI:10.1103/PhysRevLett.92.215701.

Ohashi, Y., 1984. Polysynthetically-twinned structures of enstatite and wollastonite. Physics and Chemistry of Minerals 10, 217–229. DOI:10.1007/BF00309314.

Petitgirard, S., Malfait, W.J., Journaux, B., Collings, I.E., Jennings, E.S., Blanchard, I., Kantor, I., Kurnosov, A., Cotte, M., Dane, T., Burghammer, M., Rubie, D.C., 2017. SiO_2 Glass Density to Lower-Mantle Pressures. Physical Review Letters 119, 215701. DOI:10.1103/PhysRevLett.119.215701.

Petitgirard, S., Malfait, W.J., Sinmyo, R., Kupenko, I., Hennet, L., Harries, D., Dane, T., Burghammer, M., Rubie, D.C., 2015. Fate of $MgSiO_3$ melts at core-mantle boundary conditions. Proceedings of the National Academy of Science 112, 14186–14190. DOI:10.1073/pnas.1512386112.

Prakapenka, V.P., Shen, G., Dubrovinsky, L.S., Rivers, M.L., Sutton, S.R., 2004. High pressure induced phase transformation of SiO_2 and GeO_2: difference and similarity. Journal of the Physics and Chemistry of Solids 65, 1537–1545. DOI:10.1016/j.jpcs.2003.12.019.

Richet, P., Robie, R.A., Hemingway, B.S., 1993. Entropy and structure of silicate glasses and melts. Geochimica Cosmochimica Acta 57, 2751–2766. DOI:10.1016/0016-7037(93)90388-D.

Ringwood, A.E., Major, A., 1971. Synthesis of majorite and other high pressure garnets and perovskites. Earth and Planetary Science Letters 12, 411–418. DOI:10.1016/0012-821X(71)90026-4.

Sanchez-Valle, C., Bass, J.D., 2010. Elasticity and pressure-induced structural changes in vitreous $MgSiO_3$-enstatite to lower mantle pressures. Earth and Planetary Science Letters 295, 523–530. DOI:10.1016/j.epsl.2010.04.034.

Sanloup, C., Drewitt, J.W.E., Konôpková, Z., Dalladay-Simpson, P., Morton, D.M., Rai, N., van Westrenen, W., Morgenroth, W., 2013. Structural change in molten basalt at deep mantle conditions. Nature 503, 104–107. DOI:10.1038/nature12668.

Serghiou, G., Chopelas, A., Boehler, R., 2000. Explanation of pressure-induced transformations in chain silicates based on their modular structures. Journal of Physics Condensed Matter 12, 8939–8952. DOI:10.1088/0953-8984/12/42/301.

Serghiou, G.C., Hammack, W.S., 1993. Pressure-induced amorphization of wollastonite ($CaSiO_3$) at room temperature. Journal of Chemical Physics 98, 9830–9834. DOI:10.1063/1.464361.

Shim, S.H., Catalli, K., 2009. Compositional dependence of structural transition pressures in amorphous phases with mantle-related compositions. Earth and Planetary Science Letters 283, 174–180. DOI:10.1016/j.epsl.2009.04.018.

Shim, S.H., Duffy, T.S., Shen, G., 2000. The equation of state of $CaSiO_3$ perovskite to 108 GPa at 300 K. Physics of the Earth and Plane mtary Interiors 120, 327–338. DOI:10.1016/S0031-9201(00)00154-0.

Shimizu, H., Saitoh, N., Sasaki, S., 1998. High-pressure elastic properties of liquid and solid krypton to 8 GPa. Physical Review B 57, 230–233. DOI:10.1103/PhysRevB.57.230.

Shimoda, K., Miyamoto, H., Kikuchi, M., Kusaba, K., Okuno, M., 2005. Structural evolutions of $CaSiO_3$ and $CaMgSi_2O_6$ metasilicate glasses by static compression. Chemical Geology 222, 83–93. DOI:10.1016/j.chemgeo.2005.07.003.

Smith, K.H., Shero, E., Chizmeshya, A., Wolf, G.H., 1995. The equation of state of polyamorphic

germania glass: A two-domain description of the viscoelastic response. Journal of Chemical Physics 102, 6851. DOI:10.1063/1.469122.

Soignard, E., Amin, S.A., Mei, Q., Benmore, C.J., Yarger, J.L., 2008. High-pressure behavior of As_2O_3: Amorphous-amorphous and crystalline-amorphous transitions. Physical Review B77, 144113. DOI:10.1103/PhysRevB.77.144113.

Taniguchi, T., Okuno, M., Matsumoto, T., 1997. X-ray diffraction and EXAFS studies of silicate glasses containing Mg, Ca and Ba atoms. Journal of Non-Crystalline Solids 211, 56–63. DOI:10.1016/S0022-3093(96)00632-1.

Vo-Thanh, D., Polian, A., Richet, P., 1996. Elastic properties of silicate melts up to 2350 K from Brillouin scattering. Geophysical Research Letters 23, 423–426. DOI:10.1029/96GL00308.

Whitfield, C.H., Brody, E.M., Bassett, W.A., 1976. Elastic moduli of NaCl by Brillouin scattering at high pressure in a diamond anvil cell. Review of Scientific Instruments 47, 942–947. DOI:10.1063/1.1134778.

Wolf, G.H., Wang, S., Herbst, C.A., Durben, D.J., Oliver, W.F., Kang, Z.C., Halvorson, K., 1992. Pressure induced collapse of the tetrahedral framework in crystalline and amorphous GeO_2, in: Syono, Y., Maghnani, M.H. (Eds.), High-Pressure Research: Application to Earth and Planetary Sciences. American Geophysical Union, Washington, DC. volume 67, pp. 503–517. DOI:10.1029/GM067p0503.

Yamada, A., Gaudio, S.J., Lesher, C.E., 2010. Densification of $MgSiO_3$ glass with pressure and temperature, in: Journal of Physics Conference Series, p. 012085. DOI:10.1088/1742-6596/215/1/012085.

Yan, J., Knight, J., Kunz, M., Vennila Raju, S., Chen, B., Gleason, A.E., Godwal, B.K., Geballe, Z., Jeanloz, R., Clark, S.M., 2010. The resistive-heating characterization of laser heating system and LaB_6 characterization of X-ray diffraction of beamline 12.2.2 at advanced light source. Journal of Physics and Chemistry of Solids 71, 1179–1182. DOI:10.1016/j.jpcs.2010.03.030.

Yang, H., Prewitt, C.T., 1999. Crystal structure and compressibility of a two-layer polytype of pseudowollastonite ($CaSiO_3$). American Mineralogist 84, 1902–1905. DOI:10.2138/am-1999-11-1217.

Yin, C.D., Okuno, M., Morikawa, H., Marumo, F., Yamanaka, T., 1986. Structural analysis of

$CaSiO_3$ glass by X-ray diffraction and Raman spectroscopy. Journal of Non Crystalline Solids 80, 167–174. DOI:10.1016/0022-3093(86)90391-1.

Zha, C.S., Mao, H.K., Duffy, T.S., Meade, C., 1994. Acoustic velocities and refractive index of SiO_2 glass to 57.5 GPa by Brillouin scattering. Physical Review B 50, 13105–13112.

	Max hysteresis of V_P and V_S	*Pressure of kinks in $V_P(P)$ and $V_S(P)$*	$\rho_{glass}/\rho_{crystal}$
$CaSiO_3$	7%	None	1, 0.99, or 0.92
$CaMgSi_2O_6$	-	-	0.87
$MgSiO_3$	12%	8 GPa	0.86
SiO_2	24%	3, 20 GPa	0.81

Table 1: Comparison between compression behaviors of silicate glasses in the system CaO-MgO-SiO_2. Columns list maximum hysteresis and the pressures of kinks in V_P or V_S as functions of pressure, and the ratio of densities of glass to their crystalline polymorphs at 0 GPa. The density of $CaSiO_3$ glasses are from Shimoda et al. (2005), Taniguchi et al. (1997) and Yin et al. (1986), while those of $CaMgSi_2O_6$, $MgSiO_3$ and SiO_2 glasses are from Shimoda et al. (2005), Yamada et al. (2010), and Brückner (1970), respectively. Hysteresis and kinks are from this study for $CaSiO_3$, Sanchez-Valle and Bass (2010) for $MgSiO_3$, and Zha et al. (1994) for SiO_2.

	V_P (km/s)	*V_s (km/s)*	*n*	*^{29}Si NMR shift (ppm)*
Melt-quenched glass	6.3 (±0.1)	3.4 (±0.1)	1.63 (±0.03)	-81.5
	9.3 (±0.2)	4.7 (±0.1)	1.78 (±0.05)	-
Compression-amorphized	6.3 (±0.1)	3.3 (±0.2)	1.63 (±0.03)	-
	9.6 (±0.2)	4.7 (±0.1)	1.78 (±0.05)	-
Decompression-amorphized	-	-	1.63	-81.0
References	This study	This study	This study and Kanzaki et al. (1991)	Ringwood and Major (1971)

Table 2: Properties of amorphous $CaSiO_3$ synthesized by three distinct means. All values are at room temperature, with upper and lower entries indicating measurements at ambient pressure and 41 GPa, respectively.

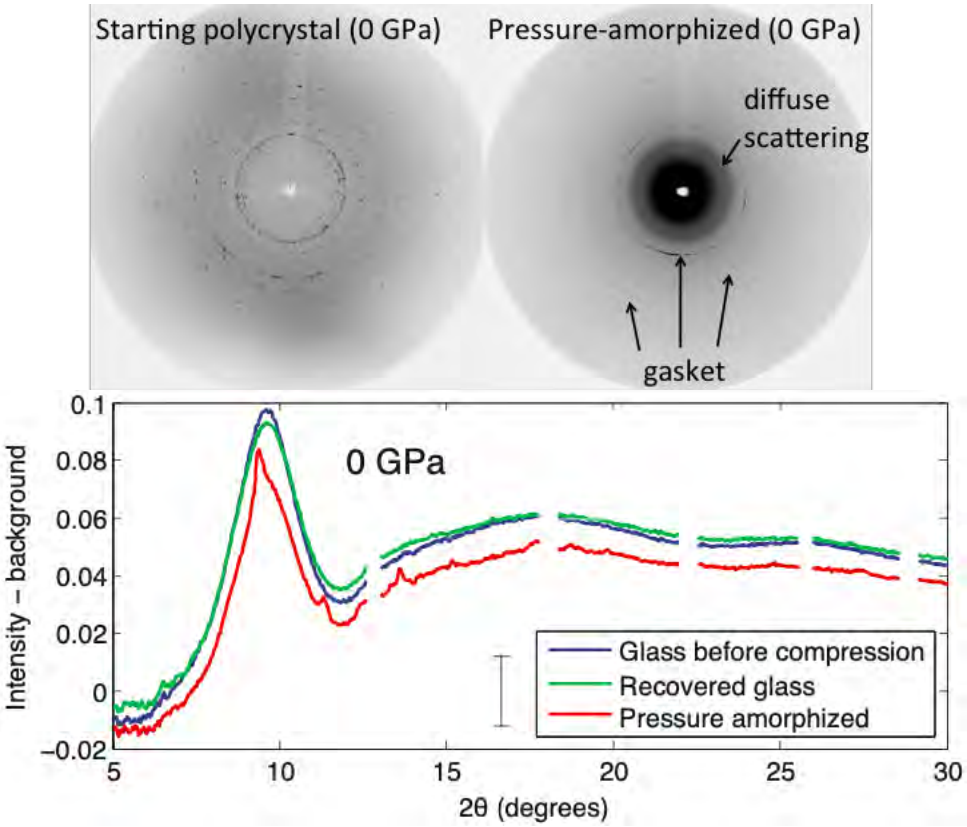

Figure 1: (Top) Raw x-ray diffraction images before and after three pressure cycles to 40 GPa showing the amorphization of polycrystalline wollastonite. (Bottom) Integrated diffraction patterns showing the similarity of structure among three amorphous samples: the melt-quenched glass before compression (blue), the same glass after two pressure cycles to 40 GPa (green), and polycrystalline wollastonite after three pressure cycles to 40 GPa (red). Gaps in integrated data are shown for angles at which diffraction from diamond or gasket obscures the data from the sample. The system background has been subtracted, and the resulting uncertainty is indicated by the error bar at bottom right.

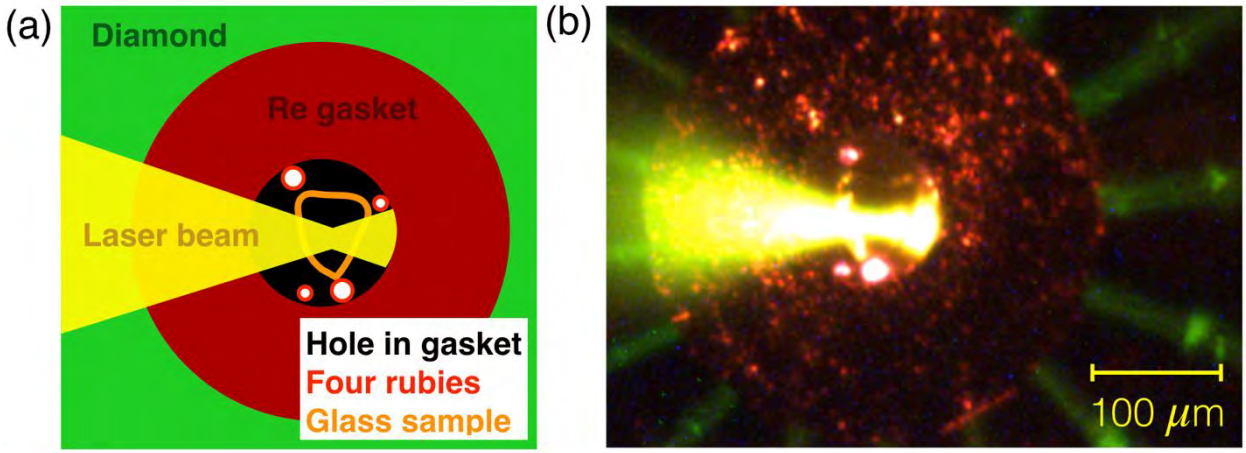

Figure 2: (a) Schematic and (b) photo of sample chamber during Brillouin experiments. A laser beam (yellow) is focused onto the $CaSiO_3$ glass sample (orange outline) inside a gasket hole compressed between diamond anvils, causing fluorescence in four rubies (red and white) located near the edge of the gasket hole. A halogen lamp illuminates the gasket (dark red). Scattered laser light illuminates the edges of the diamond facets (green). Colors in the photo have been low-pass filtered with a Kodak Wratten #22 filter, which blocks most of the elastically scattered laser light.

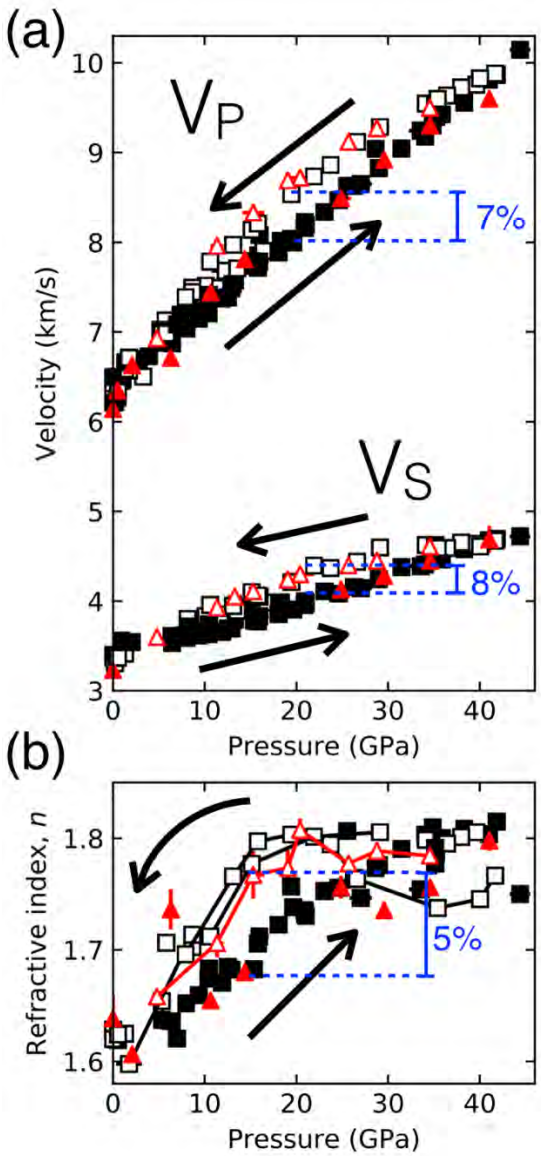

Figure 3: (a) Longitudinal (V_P) and transverse (V_S) wave velocities, and (b) index of refraction (n) of amorphous $CaSiO_3$ as a function of pressure during compression (solid symbols) and decompression (open symbols) at room temperature. Colors and shapes indicate starting material: melt-quenched $CaSiO_3$ glass (black squares), and pressure-amorphized wollastonite in a pressure-transmitting medium (red triangles). Error bars on individual data points are from scatter during rotations about the diamond-cell axis, and are approximately the same size (0.5% to 1%) as the systematic uncertainty from the Brillouin system (not shown here). Line segments connect data points during individual decompression runs in panel (b).

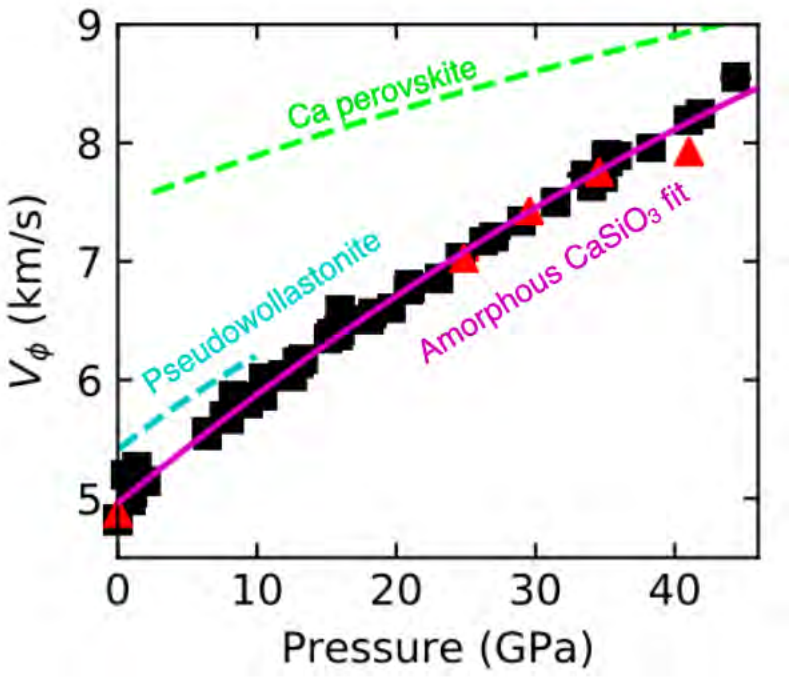

Figure 4: Bulk sound speed in amorphous $CaSiO_3$ as a function of pressure upon quasi-hydrostatic compression from 0 to 44 GPa (squares and triangles), a quadratic fit to the data (purple curve), and comparison with values for the perovskite (Shim et al., 2000) and pseudowollastonite (Yang and Prewitt, 1999) polymorphs. Colors and shapes of symbols follow Fig. 3.

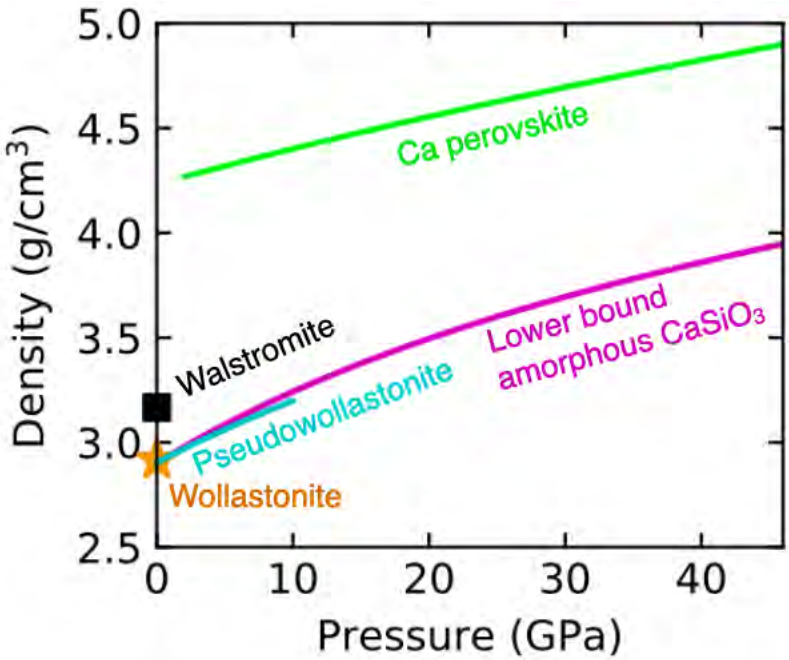

Figure 5: Pressure-density equation of state constrained here. Purple curve shows lower bound on density of amorphous $CaSiO_3$ from equation 6 using ρ_0 from Shimoda et al. (2005), and is compared to densities of crystalline forms of $CaSiO_3$: perovskite (Shim et al., 2000), walstromite (Joswig et al., 2003), wollastonite (Ohashi, 1984), and pseudowollastonite (Yang and Prewitt, 1999).

This is the peer-reviewed, final accepted version for American Mineralogist, published by the Mineralogical Society of America.
The published version is subject to change. Cite as Authors (Year) Title. American Mineralogist, in press.
DOI: https://doi.org/10.2138/am-2022-8081. http://www.minsocam.org/

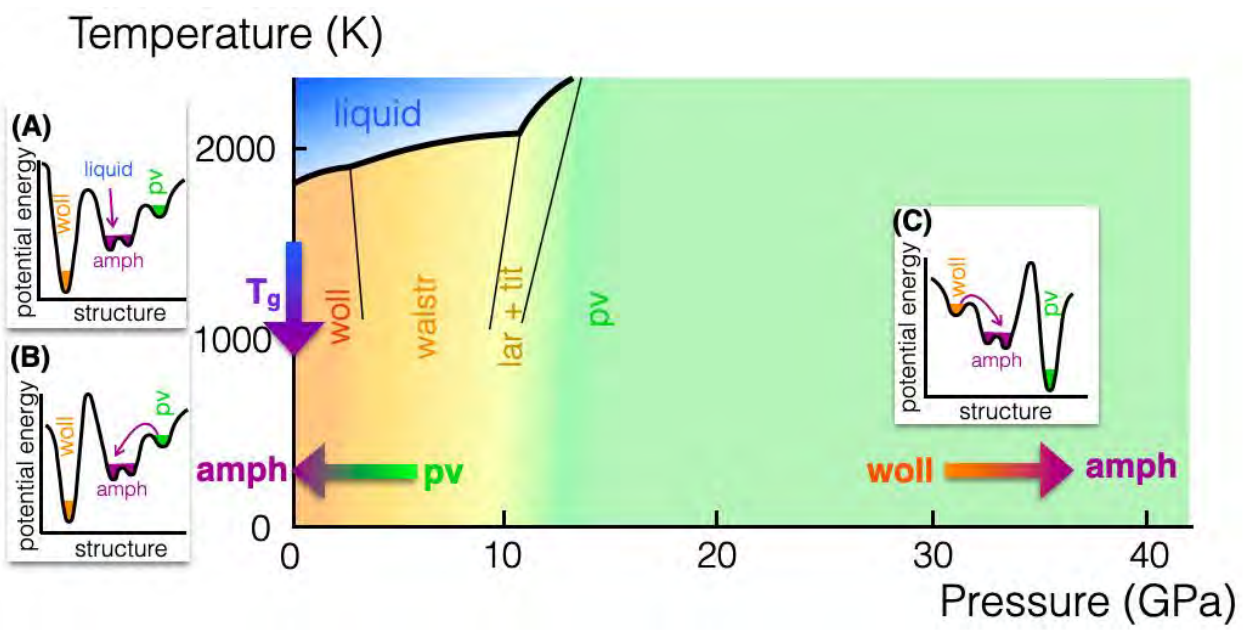

Figure 6: Equilibrium phase diagram of $CaSiO_3$ overlain by thick arrows that show three amorphization transitions. Insets A, B, and C show schematics of the potential energy landscape at conditions of each amorphization transition: (A) Melt-quenched glass formation (Vo-Thanh et al., 1996; Kubicki et al., 1992; Ringwood and Major,1971) and the glass used in this study; (B) amorphization by decompression of perovskite (Ringwood and Major,1971; Kanzaki et al., 1991); (C) amorphization by compression of wollastonite (Serghiou and Hammack, 1993) and this study. Black lines mark equilibrium phase boundaries between crystalline phases, following Akaogi et al. (2004). Colors represent different structures and phases of $CaSiO_3$: amorphous (purple), wollastonite (orange), walstromite (dark yellow), larnite plus titanite (light yellow), perovskite (green), liquid (blue).

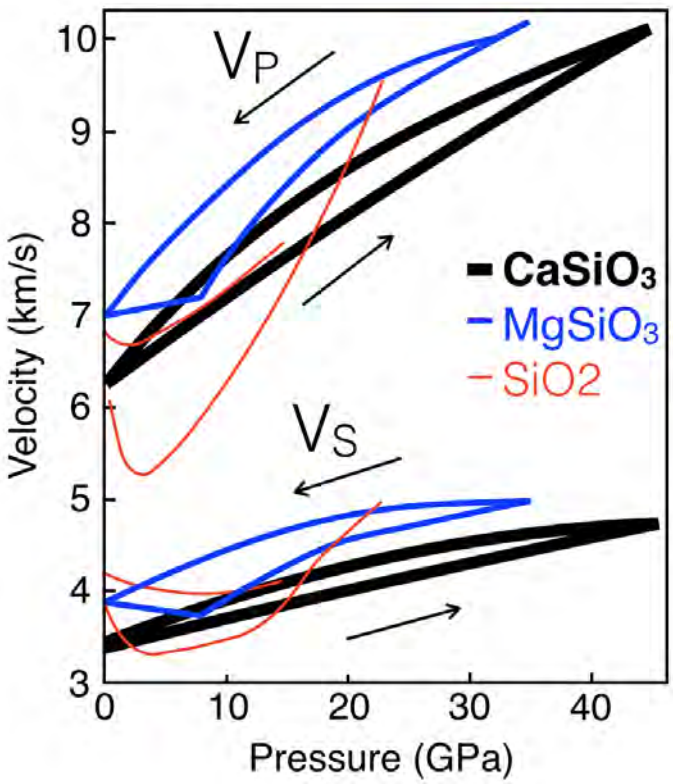

Figure 7: Comparison between sound speeds upon compression and decompression of silicate glasses in the system CaO-MgO-SiO_2. Experimental runs to maximum pressure are compared between this study ($CaSiO_3$, thick black curve), Sanchez-Valle and Bass (2010) ($MgSiO_3$, blue curve), and Zha et al. (1994) (SiO_2, thin red curve). Arrows indicate the direction of hysteresis loops. The curves for SiO_2 and $MgSiO_3$ were copied from figures in the corresponding publications. The curve for $CaSiO_3$ was generated from Fig. 3.

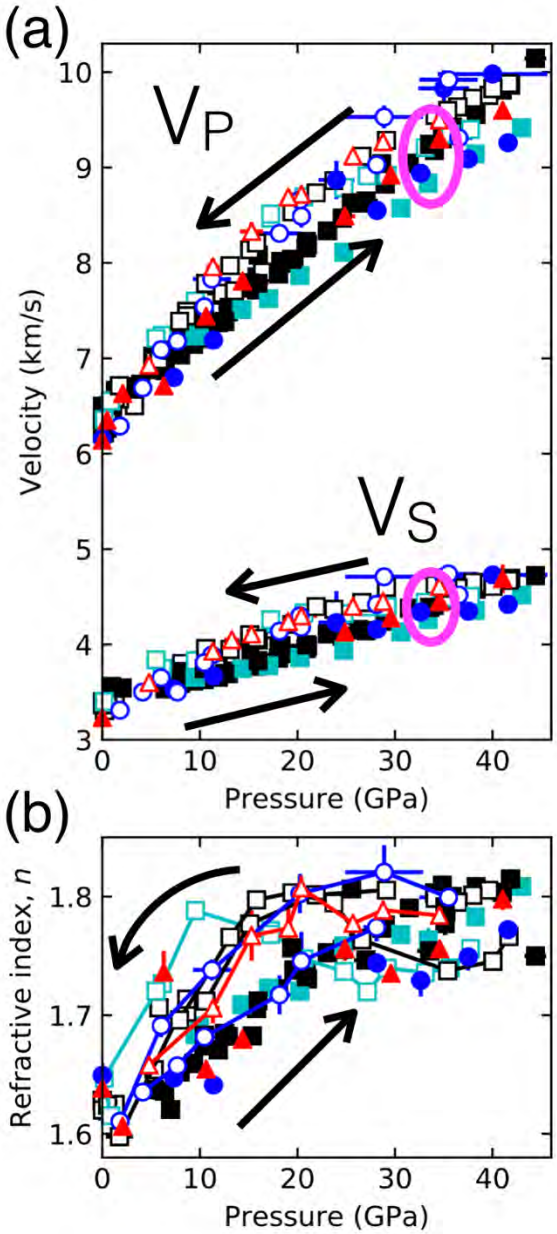

Figure 8: All sound speeds (a) and refractive indices (b) measured in the present study upon compression (solid symbols) and decompression (open symbols), as a function of pressure, including non-hydrostatically compressed samples. Black squares and red triangles represent, respectively, melt-quenched and pressure-amorphized material that is quasi-hydrostatically compressed. The powder compressed with no pressure medium is shown as blue circles, while a pressure run in which a melt-quenched glass bridged the two diamond anvils is shown in cyan squares. Sound speeds derived from the raw data of Fig. 9 are circled in pink. Line segments connect data points during individual decompression runs in panel (b).

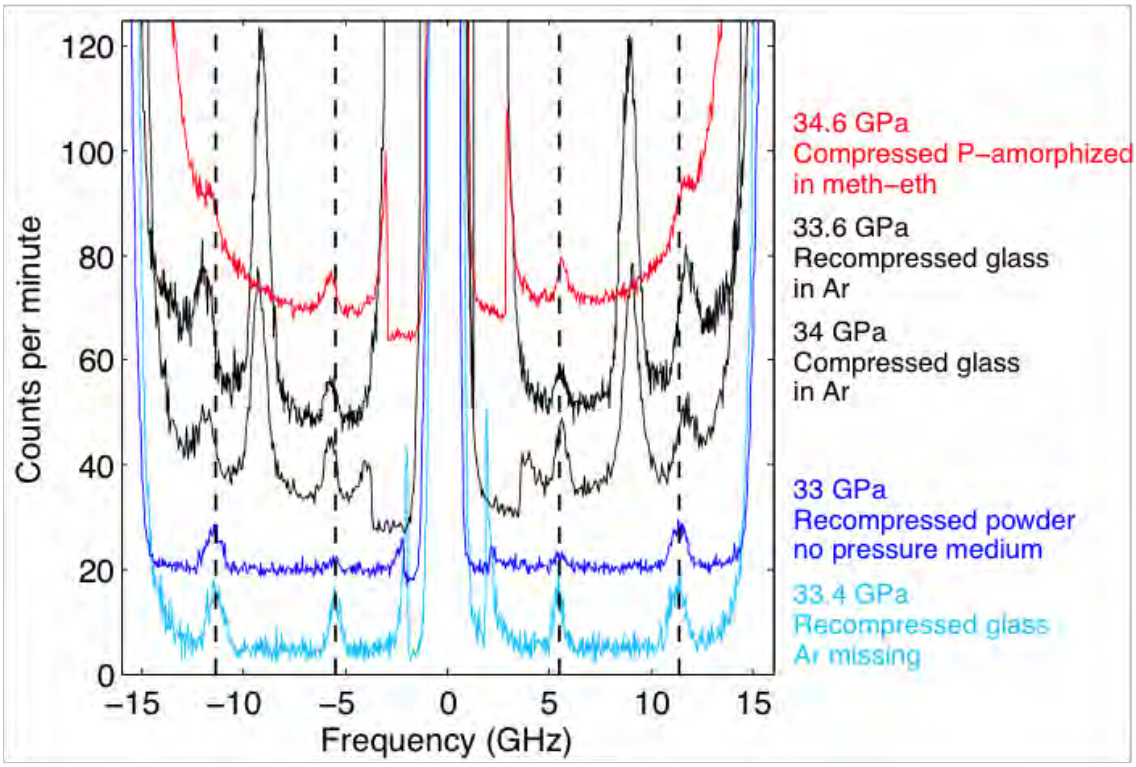

Figure 9: Brillouin spectra at 34 (±1) GPa obtained in five different compression runs that are described to the right of the figure. Photon counts are normalized to one-minute collection time, vertically offset, and plotted versus the frequency shift of the photon. Black dashed lines mark the positions of Brillouin peaks in non-hydrostatically compressed samples (both the powdered wollastonite compressed with no pressure medium, and the glass starting material that is separated from the gasket by argon but not from the diamond anvils). Black peaks at ±8 GHz are from longitudinal phonons in argon, peaks at ±16 GHz are from shear phonons in diamond, and the apparent broadening of diamond peaks in the red spectrum is caused by longitudinal phonons in methanol-ethanol.